crystals

Article

Ferroelectric SnPz/In_2Se_3 as a Stable and Durable Non-Volatile 2D Ferroelectric Memory Material

Weiwei Ren [1], Jintao Tian [2], Rui Pang [1,*] and Yuanyuan Shang [3,*]

[1] International Laboratory for Quantum Functional Materials of Henan, School of Physics and Microelectronics, Zhengzhou University, Zhengzhou 450001, China; 202012132012242@gs.zzu.edu.cn
[2] Shanghai Institute of Applied Physics, University of Chinese Academy of Sciences, Shanghai 200000, China; tianjintao199823@163.com
[3] Key Laboratory of Material Physics, Ministry of Education, School of Physics and Microelectronics, Zhengzhou University, Zhengzhou 450052, China
* Correspondence: pangrui@zzu.edu.cn (R.P.); yuanyuanshang@zzu.edu.cn (Y.S.)

Abstract: In ferroelectric memory, the repeated application of external electric fields can cause ferroelectric fatigue, limiting its stability and service life, especially as the storage unit size decreases. To address this issue, we conducted first-principles research on a SnPz/In_2Se_3 structure and examined its structure under different polarization directions. Our analysis revealed significant differences in the adsorption position of Sn atoms depending on the polarization direction, suggesting that SnPz/In_2Se_3 could be a highly stable ferroelectric storage material. Moreover, the polarization-induced changes in the electronic structure near the Fermi level, which allowed for the use of tunneling current and obtaining stored information without causing the ferroelectric fatigue effect during information readout. These findings highlight the potential of SnPz/In_2Se_3 to significantly extend the lifespan of ferroelectric materials, reduce energy consumption, and minimize the environmental impact of discarded electronic devices.

Keywords: ferroelectric; In_2Se_3; ferroelectric memory; first principles

check for updates

Citation: Ren, W.; Tian, J.; Pang, R.; Shang, Y. Ferroelectric SnPz/In_2Se_3 as a Stable and Durable Non-Volatile 2D Ferroelectric Memory Material. *Crystals* **2023**, *13*, 940. https://doi.org/10.3390/cryst13060940

Academic Editor: Pankaj Sharma

Received: 5 May 2023
Revised: 1 June 2023
Accepted: 8 June 2023
Published: 11 June 2023

1. Introduction

Storage devices play a critical role in the information age and are of great significance for human production and daily life. To develop high-performance devices, researchers have explored various materials for storage electronics, including organic materials [1–3], quantum dots [4], 2D materials [5], metal oxides [6], hybrid composite materials [7], and ferroelectric [8] and ferromagnetic materials [9]. Ferroelectric memory has numerous advantages, such as low power consumption, long durability, and fast switching, and is considered one of the candidates for the next generation of data storage devices [10].

In ferroelectric memory, the polarization states of the storage unit, such as the positions of atoms, are utilized to store binary information, resulting in stable and reliable data storage. Ferroelectric materials have high polarization and dielectric constants, making them suitable for durable data storage [10–12]. Compared to traditional storage methods, ferroelectric memory can store more information in a smaller volume, making it widely used in modern electronic devices [13,14].

The information writing and reading processes in ferroelectric memory require applying an external electric field to the storage unit. In the information reading process, the external electric field is used to detect whether the core atoms have moved. If not, it indicates that the external electric field matches the originally stored information; otherwise, if the core atoms have moved, it means that the originally stored information is different from the information specified by the external electric field. It should be noted that the original information is destroyed in this case, and need to be restored by reapplying an external voltage [15]. After multiple reading and writing processes, the repeated movement of atoms can damage the crystal structure, leading to the gradual weakening or disappearance of polarization phenomena in ferroelectric materials, known as ferroelectric fatigue phenomenon [16]. With the decreasing size of storage devices, the problem of ferroelectric fatigue has become increasingly prominent [17–19]. Reducing ferroelectric fatigue can greatly extend the lifespan of memory and enhance its stability [16,20,21]. In addition, in the current context of energy conservation and extending the lifespan of devices, reducing ferroelectric fatigue to promote the development of ferroelectric memories will help reduce energy consumption and reduce the impact of discarded electronic devices on the environment. In particular, the reading process may change the original information; if so, it is necessary to rewrite the information, creating more damage to the storage materials. Designing different reading mechanisms is crucial to promoting the development of modern ferroelectric devices.

In recent years, there has been a surge of interest in two-dimensional ferroelectric materials (2D FEs) that have reversible electric polarization, which respond to external electric fields within an extremely thin atomic layer structure [22–25]. These materials have enormous potential for applications in nanoelectronics and intelligent devices [26–34]. Among various ferroelectric two-dimensional III_2VI_3 compounds, In_2Se_3 has been extensively studied in theoretical and experimental work due to its plane and perpendicular ferroelectricity, which has been proven in experiments [26,28]. Ferroelectricity allows materials to be polarized and maintain a stable charge distribution under the effect of an external electric field, thus promoting the application of photoelectric and electroacoustic conversion, memory [35,36], and sensors [37]. Moreover, the reversible electric polarization direction of In_2Se_3 can be switched by applying an external electric field, allowing for the formation of a special "switch", thus regulating the properties of materials in a reversible manner [26,38–40]. In addition to its ferroelectricity, In_2Se_3 exhibits good photocatalytic properties, which have broad application prospects in the fields of photocatalysis, water decomposition, hydrogen energy preparation, etc. Compared with metal catalysts, In_2Se_3 has higher electrocatalytic activity and a longer life, making it an attractive alternative for photocatalytic applications [41,42].

Metal porphyrazine molecule is a complex composed of metal ions and porphyrazine molecules which are tightly bound together through coordination bonds. Porphyrazine is a large cyclic molecule composed of four pyrrole rings and four nitrogen atoms, not four benzene rings. Its structure is similar to that of porphyrin, but its chemical properties are different due to the presence of more nitrogen atoms [43–46]. Porphyrazine molecules themselves have excellent electron transfer and photocatalytic properties, and can absorb visible and near-ultraviolet light, making them widely used in photoelectric conversion and catalytic reactions [47–52]. The coordination of metal ions with porphyrazine molecules can enhance the properties of porphyrazine and endow them with new functions [49,50,52]. For example, copper porphyrazine molecules can serve as effective oxidants and act as catalysts in organic synthesis reactions; cobalt porphyrazine molecules are an important artificial photosynthetic catalyst that can decompose water into hydrogen and oxygen [50,53,54]; and the electron transfer and oxygenation properties of manganese porphyrazine molecules make them a potential biomedical research tool [49,55,56]. Furthermore, research has revealed that Sn-doped phthalocyanines possess tunable geometric and electronic structures on surfaces in the presence of the Sn atom [57,58].

This study investigates the potential of using a combination of a low-toxicity and low-melting-point metal Sn atom with SnPz to form a SnPz/In_2Se_3 structure with ferroelectricity material In_2Se_3. Using a first principles research method, the study examines and determines the structure of SnPz/In_2Se_3 under different polarization directions and analyzes the resulting geometric structure and electronic properties. The research findings demonstrate that the position of the Sn atom in adsorbed SnPz molecules varies significantly depending on the polarization direction, while remaining stable under a specific polarization direction. This indicates that SnPz/In_2Se_3 could serve as a highly stable ferroelectric memory material. Moreover, due to different charge transfer methods in different polarization states, the electronic structure of SnPz/In_2Se_3 exhibits a significant difference around the Fermi level, making it possible to detect stored information in SnPz/In_2Se_3 through measuring the tunneling current. Such a process is demonstrated by simulating the STM images under different polarizations. This approach avoids the impact of ferroelectric fatigue on the storage unit caused by the repeated application of external voltage during the information reading process. Overall, the results of this study suggest that SnPz/In_2Se_3 is a promising non-volatile ferroelectric storage material that has the potential to significantly extend the service life of ferroelectric materials, reduce energy consumption, and decrease the environmental impact of discarded electronic devices.

2. Materials and Methods

First-principles calculations based on density functional theory were carried out with the Vienna ab initio simulation package (VASP) at the level of spin-polarized generalized-gradient approximation (GGA) in the form of the Perdew–Burke–Ernzerhof (PBE) functional [59,60]. The interaction between the valence electrons and ionic cores was described within the projector-augmented wave (PAW) framework [61]. The Grimme's method (DFT-D2) was employed to incorporate the effects of van der Waals interactions [62]. An energy cutoff of 400 eV was adopted for the plane-wave basis. The electron step convergence standard was set to 1.0×10^{-4} eV, and the ion step convergence limits were set to 0.02 eV/Å force convergence standard. To minimize the interaction between adjacent SnPz molecules, a $4 \times 4 \times 1$ supercell was constructed where the distance of adjacent molecules was more than 6 Å. A vacuum space of at least 15 Å perpendicular to the layer was added to avoid spurious interactions between two neighboring sheets. The Brillouin zone was sampled by $4 \times 4 \times 1$ k-points using the Gamma centered mesh. Additionally, the k-mesh was increased to $9 \times 9 \times 1$ to obtain the density of states.

The structural stability was characterized by the binding energy (E_b), defined as $E_b = E_{SnPz} + E_{In_2Se_3} - E_{SnPz/In_2Se_3}$, here, where E_{SnPz}, $E_{In_2Se_3}$, and E_{SnPz/In_2Se_3} are the total energies of the freestanding SnPz molecules, monolayer α-In_2Se_3 supercell, and SnPz/In_2Se_3 system, respectively.

For the STM calculations, we used the Tersoff–Hamann method available in the VASP code, which is a simple model of an s-wave STM tip [63–65]:

$$n(r, E) = \sum_{\mu} |\psi_\mu(r)|^2 \delta(\varepsilon_\mu - E) \tag{1}$$

$$I(r, V) \propto \int_{E_F}^{E_F + eV} dE\, n(r, E) \tag{2}$$

In this method, the tunneling current I, which is depends on the tip position r and the applied voltage ψ_μ, is proportional to the integrated local density of states (ILDOS). The ILDOS is calculated from the Kohn—Sham eigenvectors, ψ_μ, and eigenvalues, ε_μ, where μ labels different states. E_F is the Fermi energy. In this study, a constant-height mode with an external potential of 0.5 V was applied, and the STM images were calculated within the range of 0.1 to 0.5 Å on the material surface. It should be noted that plane wave codes such as VASP may not accurately describe the exponential decay of wave functions far from atoms, and may require the extrapolation of wave functions to display physical results at large heights (such as 7 Å), otherwise non-physical effects may be displayed [66]. All the STM images were made at least 31.8 Å long in the xy plane by repeating the primitive SnPz/In_2Se_3 unit cell.

3. Results and Discussion

The tin porphyrazine molecule consists of four pyridine rings and a central tin atom, as shown in Figure 1a. From a top view, the Sn atom is located at the center of the plane. However, from a side view, the Sn atom is significantly raised relative to the porphyrazine plane, with a distance of 1.16 Å in the direction perpendicular to the macro ring from the nearest N atom. This is due to its larger atomic radius, which results in a stronger repulsion with surrounding atoms and "pushes" the Sn atom out of the porphyrazine plane. At the same time, the Sn atom also has a certain influence on the porphyrazine, ultimately causing the whole tin porphyrazine molecule to present a certain curved state.

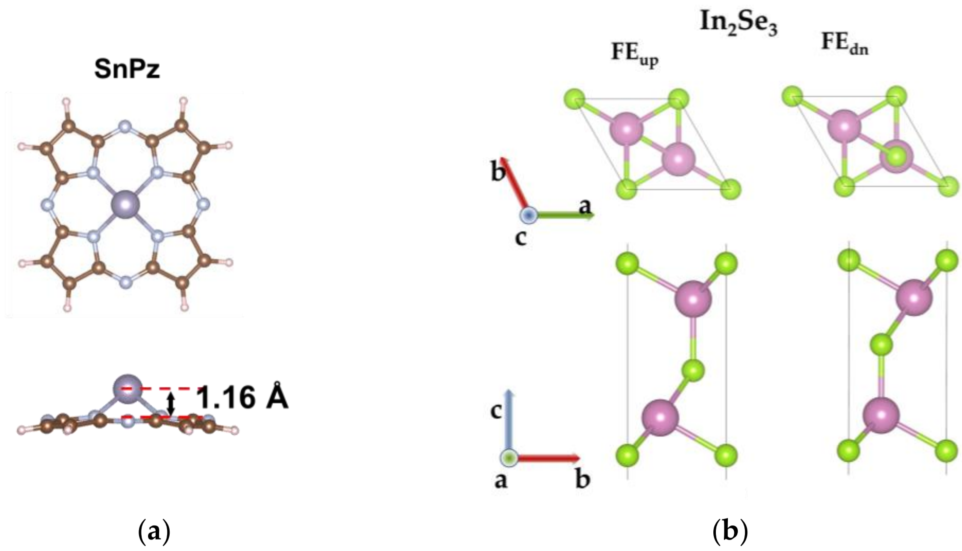

Figure 1. (**a**) The structure of SnPz molecule. (**b**) The structures of In_2Se_3 in case of FE_{up} (**left**) and FE_{dn} (**right**).

In_2Se_3 has a strong out-of-plane ferroelectricity, with its most stable phase being the α phase. In a single layer of In_2Se_3, Se and In atoms are arranged in alternating layers through covalent bonds. We optimized the unit cell of α-In_2Se_3 and calculated its lattice constant to be 4.1 Å, which was very close to previous research results [26,28]. The calculated single-layer structure of In_2Se_3 with ferroelectric polarization upward (FE_{up}) and ferroelectric polarization downward (FE_{dn}) is shown in Figure 1b.

To investigate the most stable adsorption configuration of SnPz on the surface of In_2Se_3 in different polarization states, as depicted in Figure 2a,b, by considering the relative position of the central Sn atom of SnPz to In_2Se_3, we tested eight different adsorption configurations for each case. In these configurations, the raised up (Sn-up) or sunken downward Sn atom in SnPz was located above the top layer In atom (Top1 site), above the top layer Se atom (Top2 site), above the bridge position between two adjacent top layer In atoms (Bridge site), or above the center of the triangle region in the lower right corner of the In_2Se_3 unit cell (Hollow site), respectively. The calculation results are shown in Figure 2c,d and Figure 3a, where the most stable adsorption configuration of SnPz in both FE_{up} and FE_{dn} states was with the Sn atom located above the Hollow site, corresponding to a large adsorption energy of 1.30 eV and 1.41 eV, respectively, indicating that these two adsorption structures are very stable at room temperature. Interestingly, there were significant differences in the relative positions of the Sn atom in the two polarization directions. When the system was in the FE_{up} state, the central Sn atom was in the Sn-up configuration, and the distance between the porphyrazine molecule and In_2Se_3 was 3.34 Å. When in the FE_{dn} state, the Sn atom configuration was Sn-dn, meaning that the Sn atom was located at the interface between the porphyrazine molecule and In_2Se_3. At this time, although the porphyrazine molecule was still far from the substrate (3.33 Å), the distance between the Sn atom and In_2Se_3 was only 2.13 Å, which means that the Sn atom may serve as a medium to enhance the interaction between SnPz and In_2Se_3. In summary, in the most stable structure of SnPz/In_2Se_3, the relative position of the Sn atom exhibited a significant ferroelectric dependence.

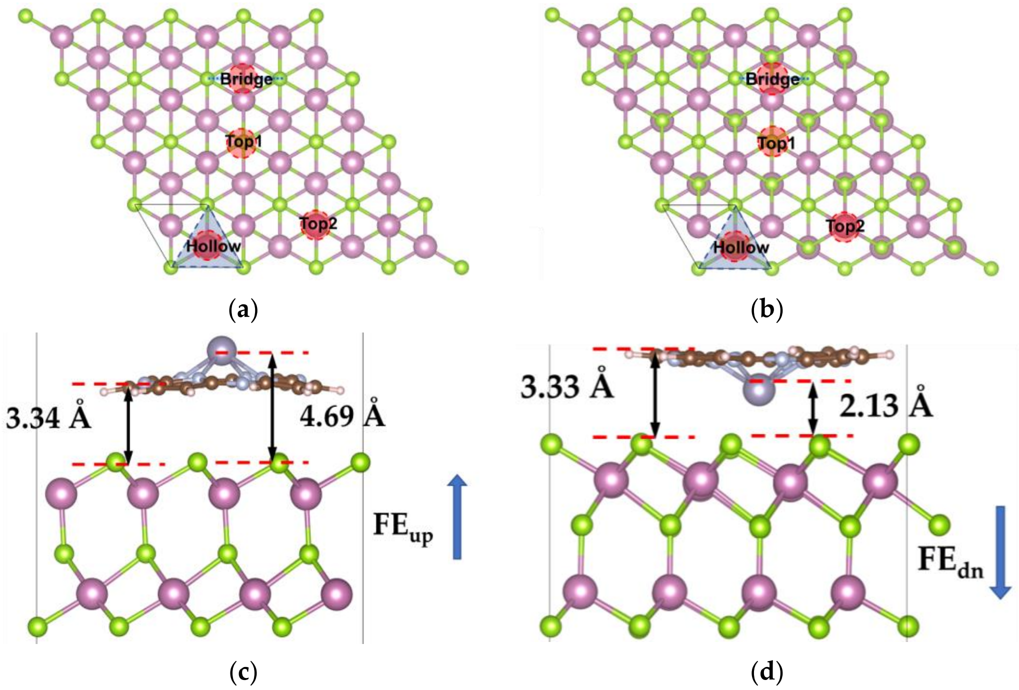

Figure 2. Different adsorption sites of SnPz molecules on the In_2Se_3 surface when the system is in the (**a**) FE_{up} and (**b**) FE_{dn} states, where each site represents the Sn atom directly above the corresponding position. (**c**) The most stable adsorption structure of the SnPz molecule when the system FE_{up} is in the FE_{up} state, where the Sn atom in SnPz is located directly above the hollow site and protrudes upward. (**d**) The most stable adsorption structure of the SnPz molecule when the system is in the FE_{dn} state, where the Sn atom in SnPz is located directly above the hollow site between the top three Se atoms and is depressed downward.

Moreover, this ferroelectric dependence was also observed in other metastable adsorption configurations. As illustrated in Figure 3a, when the system was in the FE_{up} state (black line), the Sn atom tended to form a Sn-up structure at all adsorption sites, whereas in the FE_{dn} state (red line), Sn tended to form a Sn-dn structure at all adsorption sites except for the Top1 site. Furthermore, the calculation results presented in Figure 3a indicate that, in the FE_{dn} state, the adsorption energy of SnPz on In_2Se_3 in each adsorption configuration was more stable than that in the FE_{up} state. To shed light on this phenomenon, we analyzed the PDOS of In_2Se_3, as illustrated in Figure 3b. In the original single layer In_2Se_3, when it was in the FE_{up} state, the *p* orbital of the Se atoms of top layer had an obvious occupied state at the −2.7 eV level. However, when it was in the FE_{dn} state, the *p* orbital significantly shifted upward to around −1 eV. This phenomenon prompts us to consider In_2Se_3's adsorption capacity for SnPz molecules from the perspective of the *p*-band center theory. According to the calculation of the *p*-band center, when In_2Se_3 was in the FE_{up} state the *p*-band center of the top Se atoms was situated at −2.2 eV, whereas in the FE_{dn} state, the *p*-band center significantly increased to −1.69 eV. This implies that, when In_2Se_3 and SnPz molecules are in the FE_{dn} state, a stronger bond can be formed between them, which is consistent with the calculation of the adsorption energy. In addition, the difference in adsorption energy is also related to the distribution of electrostatic potential. As shown in Figure 3c, the negative potential in SnPz molecules only existed near the Sn atom, while the Pz ring mainly exhibited positive electrostatic potential. For In_2Se_3, as shown in Figure 3d, the surface electrostatic potential in the FE_{dn} state was more positive than that in the FE_{up} state. Therefore, according to the complementary principle, when in the FE_{dn} state, the Sn atoms were more likely to adsorb on the surface of In_2Se_3.

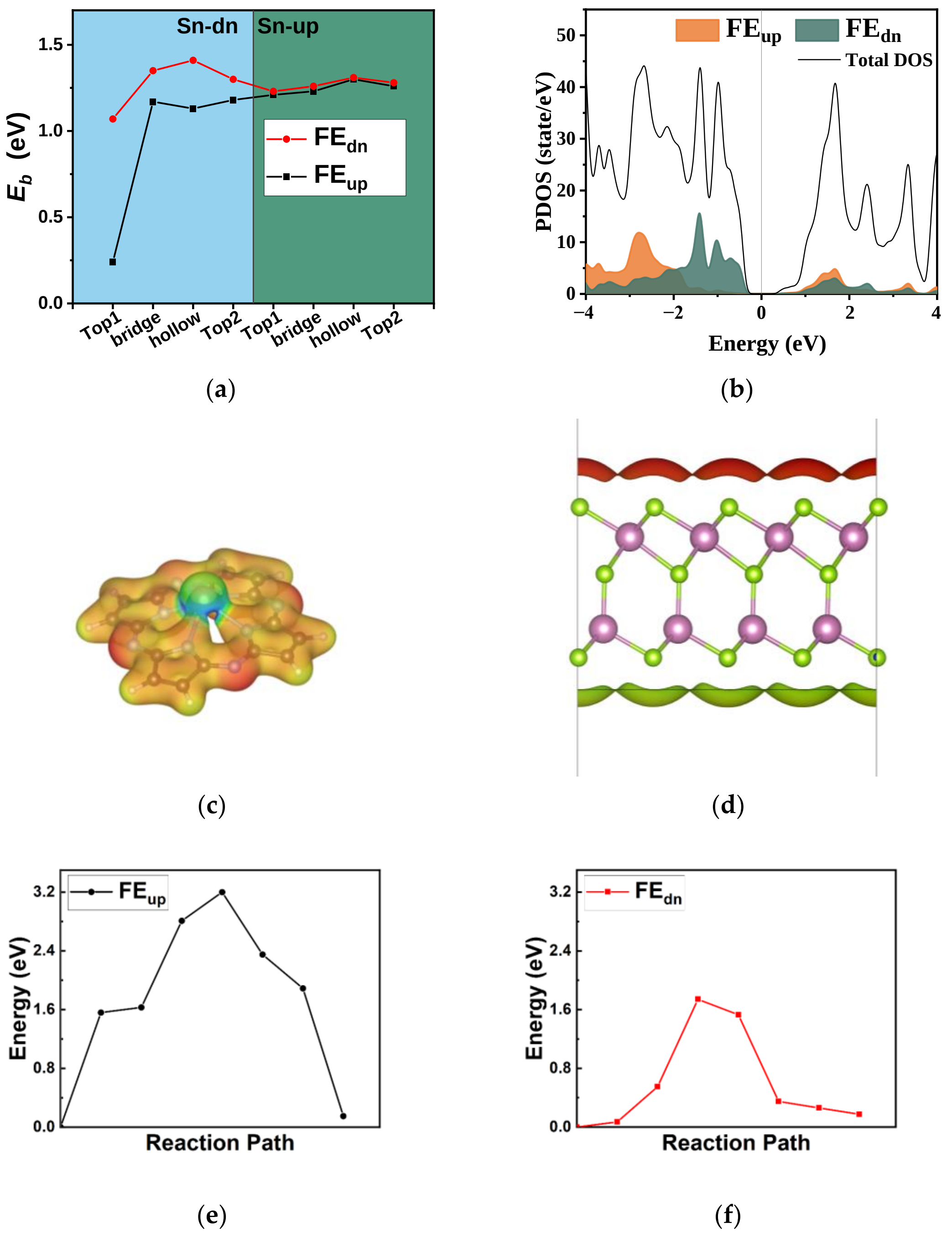

Figure 3. (**a**) Adsorption energy of SnPz molecules on In_2Se_3 surface under different adsorption configurations, where Sn-up and Sn-dn represent the upward protrusion or downward depression of the Sn atom relative to the porphyrazine ring. (**b**) PDOS of top-layer Se atoms when In_2Se_3 is in the FE_{up} and FE_{dn} states. Electrostatic potential distribution of (**c**) SnPz molecule and (**d**) In_2Se_3, in which yellow-green represents weak electrostatic potential. NEB calculation results of Sn atom migrating from the most stable position to the other side of the porphyrazine molecule in (**e**) FE_{up} and (**f**) FE_{dn} states of SnPz/In_2Se_3.

We also utilized the NEB method to further verify the stability of the Sn atom position in different polarization states. The energy barrier for the Sn atom to migrate from its stable position to the other side of the SnPz molecule under both polarization states was calculated and the results are presented in Figure 3e and 3f. The Sn atom required 3.2 eV and 1.7 eV to complete the migration process under the FE_{up} and FE_{dn} states, respectively, which exceeded the thermal fluctuations at room temperature, indicating that the Sn atom position was stable under environmental conditions. More importantly, this suggests that the polarization direction can stably regulate the structure of the adsorbed SnPz, specifically the relative position of the Sn atom. By applying a specific external electric field, the position of the Sn atom can be specified and, after the external electric field has been removed, the Sn atom cannot move to the other side of the porphyrazine molecule due to the large migration energy barrier. During this process, SnPz/In_2Se_3 stores the information left by the external electric field in the structure; that is, it completes a certain information writing process, and the written information can be stably stored even without an external electric field. This means that SnPz/In_2Se_3 is a good information carrier and has the potential to be used as a non-volatile storage unit for ferroelectric memories.

To comprehend the electronic properties of the two adsorption structures under different polarization directions, an analysis of their electronic structures was conducted. As illustrated in Figure 4a,b, the differential charge analysis revealed that in the FE_{up} state, the distance between the SnPz molecule and In_2Se_3 was large, resulting in a weak charge exchange between the porphyrazine and In_2Se_3. Conversely, in the FE_{dn} state, the Sn atom concaved downwards, significantly reducing the distance between SnPz and In_2Sn_3 (from 3.34 Å in the FE_{up} state to 2.13 Å), thereby facilitating the transfer of charges between them. As shown in Figure 4b, a charge transfer channel was formed between the Sn atom and In_2Sn_3. Both Sn and porphyrazine were evidently in a state of electron loss, and transferred electrons to three nearby Se atoms through the Sn atom. This was further corroborated through Bader charge analysis, as presented in Figure 4c. When the system was in the FE_{up} state, In_2Se_3 transferred 0.03 electrons to SnPz through the porphyrazine molecule. Conversely, in the FE_{dn} state, due to the significant electronegativity difference between Se and Sn atom (Se: 2.55, Sn: 1.96), SnPz lost 0.26 electrons to In_2Se_3 through the Sn atom. Correspondingly, in the PDOS diagram in Figure 4d, compared to the free state, a significant relative displacement of the density of states of adsorbed SnPz near the Fermi level occurred in the occupied state. In the FE_{up} state, the occupied state near the Fermi level moved downwards due to electron gain. Conversely, in the FE_{dn} state, the occupied state moved upward due to electron loss, and even produced a significant electron state occupancy at the Fermi level. In summary, by adjusting the geometric structure and charge transfer, the ferroelectric polarization can result in significantly different electronic structure of SnPz/In_2Se_3 near the Fermi level in different polarization states.

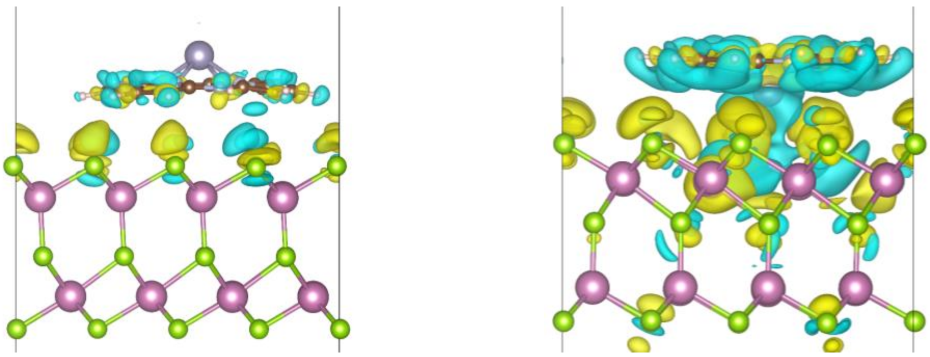

(**a**) (**b**)

Figure 4. *Cont.*

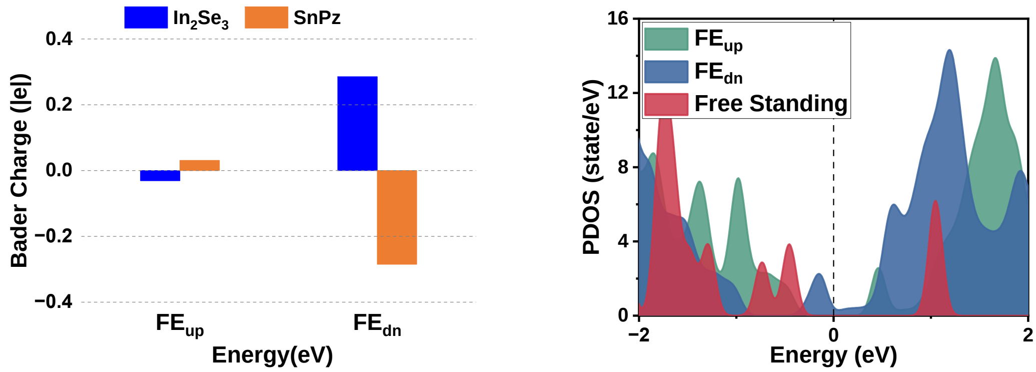

(**c**) (**d**)

Figure 4. Differential charge density map of SnPz adsorption on the In_2Se_3 surface in the (**a**) FE_{up} and (**b**) FE_{dn} states. Yellow and cyan represent electron gain and electron loss, respectively (**c**) Bader charge analysis of SnPz and In_2Se_3 under different polarization states. (**d**) Compared to the free-standing SnPz molecules, the PDOS distribution of *p* orbital of SnPz/In_2Se_3 at different polarization states.

The difference in occupation states near the Fermi level induced by ferroelectricity has an impact on the space charge distribution. As depicted in Figure 5a,b, the charge density was calculated in the range of −0.5 to 0 eV, and the results are presented under the same charge density isosurface. When the system was in the FE_{up} state, there was almost no charge distribution in the structure, especially at the interface. However, when the system was in the FE_{dn} state, the charge localization on the In_2Se_3 surface and SnPz molecule was clearly observable. The significant difference in charge distribution induced by ferroelectricity near the Fermi level makes it more suitable for interesting applications.

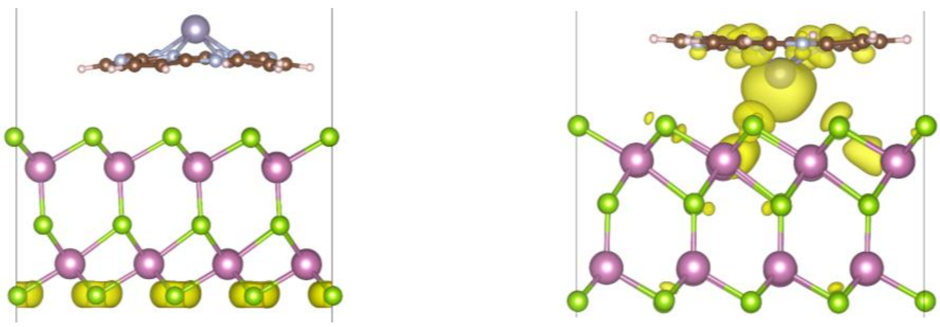

(**a**) (**b**)

Figure 5. The calculated charge density of SnPz/In_2Se_3 in the range of −0.5 to 0 eV in (**a**) FE_{up} and (**b**) FE_{dn} states, with the results displayed under the same charge density isosurface.

This charge redistribution induced by ferroelectricity reminds us that one can obtain the polarization state of the substrate directly by measuring the states of the molecule. Additionally, the states of the molecule can be measured by the tunneling current as is realized in a scanning tunneling microscope (STM). Because below the Fermi level as far as 0.5 eV, the FE_{dn} polarization generates a state on the macro-ring while the FE_{up} does not, which indicates that in bias voltage of −0.5 V, the FE_{dn} can generate tunneling current while the FE_{up} cannot. To be more specific, the STM images of structures under different polarization states were simulated, and the tunneling currents were detected at distances of 0.1 Å, 0.2 Å, 0.3 Å, 0.4 Å, and 0.5 Å on the surface of the material at a constant height mode with a bias voltage of −0.5 V. The results are displayed in Figure 6. The brightness areas suggest that significant tunneling currents were detected in the range of 0.1–0.5 Å on the surface of SnPz/In_2Se_3 in the FE_{dn} state, while no tunneling current was observed at all in the FE_{up} state. This characteristic makes the $SnPz/In_2Se_3$ system highly promising for ferroelectric memories. In $SnPz/In_2Se_3$, the presence of a tunneling current at a bias voltage of −0.5 V could be detected to obtain the stored information in the structure, thereby avoiding the repeated application of external voltage to the structure during information readout, which greatly extends the life of the memory by reduce ferroelectric fatigue.

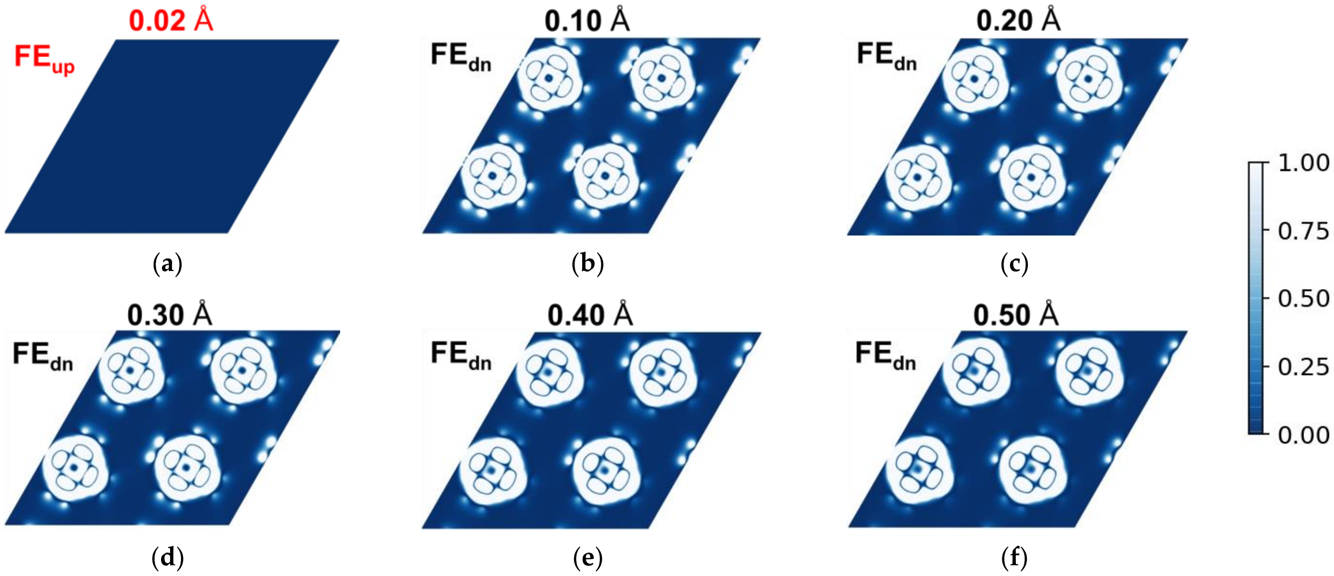

Figure 6. (**a**) STM image of $SnPz/In_2Se_3$ in the FE_{up} state, taking the result at the material surface of 0.2 Å as an example. (**b**–**f**) STM images of $SnPz/In_2Se_3$ in the FE_{dn} state, with probe heights of 0.1 Å, 0.2 Å, 0.3 Å, 0.4 Å, and 0.5 Å from the $SnPz/In_2Se_3$ surface, respectively.

There are many examples of porphyrazine-type molecules on various kinds of surface substrate. For example, in 1998 it was reported that zinc porphyrazine (ZnPz) could be successfully adsorbed onto Y-zeolite by stirring calcinated zeolite in freshly distilled pyridine [67]. In 2017, two rounds of ultrasonic treatment in THF were used to fix zinc pyrene-porphyrazine conjugate (ZnPzPy) and ZnPz onto a graphene substrate [68]. Additionally, CoPz has also been successfully immobilized on the oxygen vacancy-containing SnO_2 surface [54]. In addition, various metal porphyrazine derivatives have been successfully immobilized on Au (111) surface [69–71] and ZnO surface [72]. In recent years, there has been increasing theoretical research on anchoring metal porphyrazine onto various two-dimensional materials for use as catalysts, magnetic storage devices, sensors, and optoelectronic devices [38,50]. Based on the above research work, there might be two methods for obtaining porphyrazine adsorbed on a substrate. One is via synthesizing the porphyrazine molecules in solution and evaporating them in some vacuum environment and letting them deposit on the substrate. The other is via depositing pyrrole-derivation molecules and using some annealing techniques to make them take offside chains to form porphyrazine. Considering that the stability of 2D materials are usually low, maybe the first one is suitable for our case.

4. Conclusions

In this work, we used cheap and low toxicity SnPz molecules and the classic ferroelectric material In_2Se_3 to construct $SnPz/In_2Se_3$ structures. We fully considered various configurations of SnPz molecules adsorbed on the In_2Se_3 substrate in different polarization states. The results showed that when In_2Se_3 was in the FE_{dn} state, the *p*-band center of the top layer Se atom was obviously closer to the Fermi energy level than that in FE_{up} state, which enhanced the adsorption capacity for SnPz. Moreover, the placement of the Sn atom within SnPz molecules significantly affected the adsorption energy. In the FE_{up} state, Sn atoms are inclined towards being situated above the porphyrazine molecules, whereas in the FE_{dn} state they are more likely to be between the porphyrazine molecules and In_2Se_3. The ferroelectric dependence of the relative position of the Sn atom indicates the potential of SnPz/In_2Se_3 as a ferroelectric memory. Simultaneously, due to the diverse relative positions of the Sn atom in various polarization directions, there exists a substantial variation in charge transfer between SnPz and In_2Se_3. This variation results in the occupied state position near the Fermi level of the SnPz molecule moving in the opposite direction in FE_{up} and FE_{dn} states, leading to a significant difference in the electronic structure near the Fermi energy level. Further calculations confirm that this difference in the occupation state of SnPz results in significant differences in the charge density and tunneling current of SnPz/In_2Se_3 in different electric polarization states. Consequently, it is feasible to read stored information from the structure by detecting tunneling current. In conclusion, our calculations show that the structural changes and the differences in electronic structures of SnPz/In_2Se_3 induced by ferroelectricity make it not only a novel, non-volatile ferroelectric memory material, but also allow for the utilization of tunnel current to extract information from the structure and reduce ferroelectric fatigue caused by the repeated application of external voltage to storage cells. These characteristics are expected to greatly enhance the stability and durability of ferroelectric memories in practical use.

Author Contributions: Conceptualization, W.R. and R.P.; methodology, R.P.; software, W.R.; validation, W.R. and J.T.; formal analysis, W.R. and R.P.; investigation, W.R. and J.T.; resources, R.P. and Y.S.; data curation, W.R. and J.T.; writing—original draft preparation, W.R.; writing—review and editing, R.P. and Y.S.; visualization, W.R.; supervision, R.P. and Y.S.; project administration, R.P.; funding acquisition, R.P. and Y.S. All authors have read and agreed to the published version of the manuscript.

Funding: This research was funded by the National Natural Science Foundation of China (11704342, 51872267); the China Postdoctoral Science Foundation (2019M652559); the Natural Science Foundation of Henan province, China (202300410371); the Program for Science and Technology Innovation Talents in Universities of Henan Province (No. 21HASTIT017); Zhengzhou University 2022 Young Teachers' Fund for Basic Research Cultivation (JC22149002); the Henan Province Key Research Project Plan for Higher Education Institutions (23A140005).

Data Availability Statement: Not applicable.

Acknowledgments: Thank you to all the collaborators on the paper for their contributions, Pang Rui for his guidance, and the Zhengzhou National Supercomputing Center for providing computational support.

Conflicts of Interest: The authors declare no conflict of interest.

References

1. Lv, Z.; Hu, Q.; Xu, Z.-X.; Wang, J.; Chen, Z.; Wang, Y.; Chen, M.; Zhou, K.; Zhou, Y.; Han, S.-T. Organic memristor utilizing copper phthalocyanine nanowires with infrared response and cation regulating properties. *Adv. Electron. Mater.* **2019**, *5*, 1800793. [CrossRef]
2. Au-Duong, A.-N.; Kuo, C.-C.; Chiu, Y.-C. Self-assembled oligosaccharide-based block copolymers as charge-storage materials for memory devices. *Polym. J.* **2018**, *50*, 649–658. [CrossRef]
3. Yu, Y.; Ma, Q.; Ling, H.; Li, W.; Ju, R.; Bian, L.; Shi, N.; Qian, Y.; Yi, M.; Xie, L.; et al. Small-molecule-based organic field-effect transistor for nonvolatile memory and artificial synapse. *Adv. Funct. Mater.* **2019**, *29*, 1904602. [CrossRef]
4. Wang, Y.; Lv, Z.; Liao, Q.; Shan, H.; Chen, J.; Zhou, Y.; Zhou, L.; Chen, X.; Roy, V.A.L.; Wang, Z.; et al. Synergies of electrochemical metallization and valence change in all-inorganic perovskite quantum dots for resistive switching. *Adv. Mater.* **2018**, *30*, 1800327. [CrossRef]
5. Wang, M.; Cai, S.; Pan, C.; Wang, C.; Lian, X.; Zhuo, Y.; Xu, K.; Cao, T.; Pan, X.; Wang, B.; et al. Robust memristors based on layered two-dimensional materials. *Nat. Electron.* **2018**, *1*, 130–136. [CrossRef]
6. Russo, P.; Xiao, M.; Liang, R.; Zhou, N.Y. UV-induced multilevel current amplification memory effect in zinc oxide rods resistive switching devices. *Adv. Funct. Mater.* **2018**, *28*, 1706230. [CrossRef]
7. Lee, L.; Hwang, J.; Jung, J.W.; Kim, J.; Lee, H.-I.; Heo, S.; Yoon, M.; Choi, S.; Van Long, N.; Park, J.; et al. ZnO composite nanolayer with mobility edge quantization for multi-value logic transistors. *Nat. Commun.* **2019**, *10*, 1998. [CrossRef]
8. Chanthbouala, A.; Garcia, V.; Cherifi, R.O.; Bouzehouane, K.; Fusil, S.; Moya, X.; Xavier, S.; Yamada, H.; Deranlot, C.; Mathur, N.D.; et al. A ferroelectric memristor. *Nat. Mater.* **2012**, *11*, 860–864. [CrossRef]

9. Kurenkov, A.; DuttaGupta, S.; Zhang, C.; Fukami, S.; Horio, Y.; Ohno, H. Artificial neuron and synapse realized in an antiferromagnet/ferromagnet heterostructure using dynamics of spin-orbit torque switching. *Adv. Mater.* **2019**, *31*, 1900636. [CrossRef] [PubMed]
10. Scott, J.F. Applications of modern ferroelectrics. *Science* **2007**, *315*, 954–959. [CrossRef]
11. Wang, D.-S. Impact of forming gas annealing on the dielectric properties of $SrBi_2Ta_2O_9$ thin films prepared by metalorganic decomposition. *J. Appl. Phys.* **2012**, *112*, 084104. [CrossRef]
12. Roy, A.; Maity, S.; Dhar, A.; Bhattacharya, D.; Ray, S. Temperature dependent leakage current behavior of pulsed laser ablated $SrBi_2Ta_2O_9$ thin films. *J. Appl. Phys.* **2009**, *105*, 044103. [CrossRef]
13. Banerjee, W. Challenges and applications of emerging nonvolatile memory devices. *Electronics* **2020**, *9*, 1029. [CrossRef]
14. Arimoto, Y.; Ishiwara, H. Current status of ferroelectric random-access memory. *MRS Bull.* **2004**, *29*, 823–828. [CrossRef]
15. Scott, J.F.; Paz de Araujo, C.A. Ferroelectric memories. *Science* **1989**, *246*, 1400–1405. [CrossRef] [PubMed]
16. Tagantsev, A.K.; Stolichnov, I.; Colla, E.L.; Setter, N. Polarization fatigue in ferroelectric films: Basic experimental findings, phenomenological scenarios, and microscopic features. *J. Appl. Phys.* **2001**, *90*, 1387–1402. [CrossRef]
17. Ihlefeld, J.F.; Harris, D.T.; Keech, R.; Jones, J.L.; Maria, J.-P.; Trolier-McKinstry, S. Scaling effects in perovskite ferroelectrics: Fundamental limits and process-structure-property relations. *J. Am. Ceram. Soc.* **2016**, *99*, 2537–2557. [CrossRef]
18. Junquera, J.; Ghosez, P. Critical thickness for ferroelectricity in perovskite ultrathin films. *Nature* **2003**, *422*, 506–509. [CrossRef]
19. Kim, D.J.; Jo, J.Y.; Kim, Y.S.; Chang, Y.J.; Lee, J.S.; Yoon, J.-G.; Song, T.K.; Noh, T.W. Polarization relaxation induced by a depolarization field in ultrathin ferroelectric $BaTiO_3$ capacitors. *Phys. Rev. Lett.* **2005**, *95*, 237602. [CrossRef]
20. de Araujo, C.A.P.; Cuchiaro, J.D.; McMillan, L.D.; Scott, M.C.; Scott, J.F. Fatigue-free ferroelectric capacitors with platinum electrodes. *Nature* **1995**, *374*, 627–629. [CrossRef]
21. Goux, L.; Russo, G.; Menou, N.; Lisoni, J.G.; Schwitters, M.; Paraschiv, V.; Maes, D.; Artoni, C.; Corallo, G.; Haspeslagh, L.; et al. A highly reliable 3D integrated SBT ferroelectric capacitor enabling FeRAM scaling. *IEEE Trans. Electron Devices* **2005**, *52*, 447–453. [CrossRef]
22. Chang, K.; Liu, J.; Lin, H.; Wang, N.; Zhao, K.; Zhang, A.; Jin, F.; Zhong, Y.; Hu, X.; Duan, W.; et al. Discovery of robust in-plane ferroelectricity in atomic-thick SnTe. *Science* **2016**, *353*, 274–278. [CrossRef] [PubMed]
23. Wu, M.; Zeng, X.C. Intrinsic ferroelasticity and/or multiferroicity in two-dimensional phosphorene and phosphorene analogues. *Nano Lett.* **2016**, *16*, 3236–3241. [CrossRef]
24. Fei, R.; Kang, W.; Yang, L. Ferroelectricity and phase transitions in monolayer group-IV monochalcogenides. *Phys. Rev. Lett.* **2016**, *117*, 097601. [CrossRef] [PubMed]
25. Mehboudi, M.; Fregoso, B.M.; Yang, Y.; Zhu, W.; Van Der Zande, A.; Ferrer, J.; Bellaiche, L.; Kumar, P.; Barraza-Lopez, S. Structural phase transition and material properties of few-layer monochalcogenides. *Phys. Rev. Lett.* **2016**, *117*, 246802. [CrossRef] [PubMed]
26. Ding, W.; Zhu, J.; Wang, Z.; Gao, Y.; Xiao, D.; Gu, Y.; Zhang, Z.; Zhu, W. Prediction of intrinsic two-dimensional ferroelectrics in In_2Se_3 and other III_2 -VI_3 van der Waals materials. *Nat. Commun.* **2017**, *8*, 14956. [CrossRef]
27. Wang, H.; Qian, X. Two-dimensional multiferroics in monolayer group IV monochalcogenides. *2D Mater.* **2017**, *4*, 015042. [CrossRef]
28. Cui, C.; Hu, W.J.; Yan, X.; Addiego, C.; Gao, W.; Wang, Y.; Wang, Z.; Li, L.; Cheng, Y.; Li, P.; et al. Intercorrelated in-plane and out-of-plane ferroelectricity in ultrathin two-dimensional layered semiconductor In_2Se_3. *Nano Lett.* **2018**, *18*, 1253–1258. [CrossRef]
29. Xu, B.; Xiang, H.; Xia, Y.; Jiang, K.; Wan, X.; He, J.; Yin, J.; Liu, Z. Monolayer $AgBiP_2Se_6$: An atomically thin ferroelectric semiconductor with out-plane polarization. *Nanoscale* **2017**, *9*, 8427–8434. [CrossRef]
30. Fei, Z.; Zhao, W.; Palomaki, T.A.; Sun, B.; Miller, M.K.; Zhao, Z.; Yan, J.; Xu, X.; Cobden, D.H. Ferroelectric switching of a two-dimensional metal. *Nature* **2018**, *560*, 336–339. [CrossRef]
31. Zhou, Y.; Wu, D.; Zhu, Y.; Cho, Y.; He, Q.; Yang, X.; Herrera, K.; Chu, Z.; Han, Y.; Downer, M.C.; et al. Out-of-plane piezoelectricity and ferroelectricity in layered α-In_2Se_3 nanoflakes. *Nano Lett.* **2017**, *17*, 5508–5513. [CrossRef]
32. Xiao, J.; Zhu, H.; Wang, Y.; Feng, W.; Hu, Y.; Dasgupta, A.; Han, Y.; Wang, Y.; Muller, D.A.; Martin, L.W.; et al. Intrinsic two-dimensional ferroelectricity with dipole locking. *Phys. Rev. Lett.* **2018**, *120*, 227601. [CrossRef]
33. Heron, J.T.; Bosse, J.L.; He, Q.; Gao, Y.; Trassin, M.; Ye, L.; Clarkson, J.D.; Wang, C.; Liu, J.; Salahuddin, S.; et al. Deterministic switching of ferromagnetism at room temperature using an electric field. *Nature* **2014**, *516*, 370–373. [CrossRef]
34. Scott, J.F. Data storage: Multiferroic memories. *Nat. Mater.* **2007**, *6*, 256–257. [CrossRef]
35. Hou, P.; Xing, S.; Liu, X.; Chen, C.; Zhong, X.; Wang, J.; Ouyang, X. Resistive switching behavior in α-In_2Se_3 nanoflakes modulated by ferroelectric polarization and interface defects. *RSC Adv.* **2019**, *9*, 30565–30569. [CrossRef]
36. Wan, S.; Li, Y.; Li, W.; Mao, X.; Wang, C.; Chen, C.; Dong, J.; Nie, A.; Xiang, J.; Liu, Z.; et al. Nonvolatile ferroelectric memory effect in ultrathin α-In_2Se_3. *Adv. Funct. Mater.* **2019**, *29*, 1808606. [CrossRef]
37. Tang, X.; Shang, J.; Gu, Y.; Du, A.; Kou, L. Reversible gas capture using a ferroelectric switch and 2D molecule multiferroics on the In_2Se_3 monolayer. *J. Mater. Chem. A* **2020**, *8*, 7331–7338. [CrossRef]
38. Tang, X.; Shang, J.; Ma, Y.; Gu, Y.; Chen, C.; Kou, L. Tuning magnetism of metal porphyrazine molecules by a ferroelectric In_2Se_3 monolayer. *ACS Appl. Mater. Interfaces* **2020**, *12*, 39561–39566. [CrossRef]
39. Zhu, Z.; Zhang, B.; Chen, X.; Qian, X.; Qi, J. Electric field control of molecular magnetic state by two-dimensional ferroelectric heterostructure engineering. *Appl. Phys. Lett.* **2020**, *117*, 082902. [CrossRef]

40. Wang, X.; Xiao, C.; Yang, C.; Chen, M.; Yang, S.A.; Hu, J.; Ren, Z.; Pan, H.; Zhu, W.; Xu, Z.-A.; et al. Ferroelectric control of single-molecule magnetism in 2D limit. *Sci. Bull.* **2020**, *65*, 1252–1259. [CrossRef]
41. Ju, L.; Tan, X.; Mao, X.; Gu, Y.; Smith, S.; Du, A.; Chen, Z.; Chen, C.; Kou, L. Controllable CO_2 electrocatalytic reduction via ferroelectric switching on single atom anchored In_2Se_3 monolayer. *Nat. Commun.* **2021**, *12*, 5128. [CrossRef]
42. Kim, H.S. Computational design of a switchable heterostructure electrocatalyst based on a two-dimensional ferroelectric In_2Se_3 material for the hydrogen evolution reaction. *J. Mater. Chem. A* **2021**, *9*, 11553–11562. [CrossRef]
43. Wang, Z.; Day, P.N.; Pachter, R. Density functional theory studies of meso-alkynyl porphyrins. *J. Chem. Phys.* **1998**, *108*, 2504–2510. [CrossRef]
44. Beljonne, D.; O'Keefe, G.E.; Hamer, P.J.; Friend, R.H.; Anderson, H.L.; Brédas, J.L. Investigation of the linear and nonlinear optical response of edge-linked conjugated zinc porphyrin oligomers by optical spectroscopy and configuration interaction techniques. *J. Chem. Phys.* **1997**, *106*, 9439–9460. [CrossRef]
45. Chen, P.; Tomov, I.V.; Dvornikov, A.S.; Nakashima, M.; Roach, J.F.; Alabran, D.M.; Rentzepis, P.M. Picosecond kinetics and reverse saturable absorption of meso-substituted tetrabenzoporphyrins. *J. Phys. Chem.* **1996**, *100*, 17507–17512. [CrossRef]
46. Henari, F.Z.; Blau, W.J.; Milgrom, L.R.; Yahioglu, G.; Phillips, D.; Lacey, J.A. Third-order optical non-linearity in Zn(II) complexes of 5,10,15,20-tetraarylethynyl-substituted porphyrins. *Chem. Phys. Lett.* **1997**, *267*, 229–233. [CrossRef]
47. Petrov, O.A. Regularities of the catalytic influence of organic base on the formation of magnesium and zinc complexes of porphyrazines. *Russ. Chem. Bull.* **2022**, *71*, 613–619. [CrossRef]
48. Im, Y.K.; Lee, D.G.; Noh, H.J.; Yu, S.Y.; Mahmood, J.; Lee, S.Y.; Baek, J.B. Crystalline porphyrazine-linked fused aromatic networks with high proton conductivity. *Angew. Chem. Int. Edit.* **2022**, *61*, e202203250. [CrossRef] [PubMed]
49. Leda, A.; Hassani, M.; Rebis, T.; Falkowski, M.; Piskorz, J.; Mlynarczyk, D.T.; McNeice, P.; Milczarek, G. Improved electrochemical hydrogen peroxide detection using a nickel(II) phthalimide-substituted porphyrazine combined with various carbon nanomaterials. *Nanomaterials* **2023**, *13*, 862. [CrossRef]
50. Silva, H.N.; Toma, S.H.; Hennemann, A.L.; Gonçalves, J.M.; Nakamura, M.; Araki, K.; Toyama, M.M.; Toma, H.E. A new supramolecular tetraruthenated cobalt(II) porphyrazine displaying outstanding electrocatalytical performance in oxygen evolution reaction. *Molecules* **2022**, *27*, 4598. [CrossRef] [PubMed]
51. Yagodin, A.V.; Mikheev, I.A.; Bunin, D.A.; Sinelshchikova, A.A.; Martynov, A.G.; Gorbunova, Y.G.; Tsivadze, A.Y. Tetraquinoxalinoporphyrazine–π-extended NIR-absorbing photosensitizer with improved photostability. *Dyes Pigm.* **2023**, *216*, 111326. [CrossRef]
52. Koczorowski, T.; Szczolko, W.; Bakun, P.; Wicher, B.; Sobotta, L.; Gdaniec, M.; Teubert, A.; Mielcarek, J.; Tykarska, E.; Korecki, J.; et al. The valence and spin state tuning of iron(II/III) porphyrazines with bulky pyrrolyl periphery in solution and solid state. *Molecules* **2022**, *27*, 7820. [CrossRef] [PubMed]
53. Malyasova, A.S.; Smirnova, P.N.; Koifman, O.I. Complexation of benzoannelated porphyrazines with zinc(II) and cobalt(II) acetates in pyridine. *Russ. J. Inorg. Chem.* **2022**, *67*, 388–394. [CrossRef]
54. Zhang, Q.; Yang, C.; Zhang, B.; Deng, K. Cobalt porphyrazine supported on SnO_2 with oxygen vacancies for boosting photocatalytic aerobic oxidation of glucose to organic acids in an aqueous medium. *ACS Sustain. Chem. Eng.* **2021**, *9*, 2057–2066. [CrossRef]
55. Ristori, S.; Ricciardi, G.; Pietrangeli, D.; Rosa, A.; Feis, A. Hydrotropic solubilization of gold nanoparticles functionalized with proto-alkylthioporphyrazines. *J. Phys. Chem. C* **2009**, *113*, 8537–8540. [CrossRef]
56. Falkowski, M.; Leda, A.; Rebis, T.; Piskorz, J.; Popenda, L.; Hassani, M.; Mlynarczyk, D.T.; Marszall, M.P.; Milczarek, G. A synergistic effect of phthalimide-substituted sulfanyl porphyrazines and carbon nanotubes to improve the electrocatalytic detection of hydrogen peroxide. *Molecules* **2022**, *27*, 4409. [CrossRef]
57. Baran, J.D.; Larsson, J.A. Structure and energetics of shuttlecock-shaped tin-phthalocyanine on Ag(111): A density functional study employing dispersion correction. *J. Phys. Chem. C* **2012**, *116*, 9487–9497. [CrossRef]
58. Wang, Y.; Ge, X.; Manzano, C.; Kröger, J.; Berndt, R.; Hofer, W.A.; Tang, H.; Cerda, J. Supramolecular patterns controlled by electron interference and direct intermolecular interactions. *J. Am. Chem. Soc.* **2009**, *131*, 10400–10402. [CrossRef]
59. Kresse, G.; Furthmüller, J. Efficient iterative schemes for ab initio total-energy calculations using a plane-wave basis set. *Phys. Rev. B* **1996**, *54*, 11169–11186. [CrossRef]
60. Perdew, J.P.; Burke, K.; Ernzerhof, M. Generalized Gradient Approximation Made Simple. *Phys. Rev. Lett.* **1996**, *77*, 3865–3868. [CrossRef]
61. Blöchl, P.E. Projector augmented-wave method. *Phys. Rev. B* **1994**, *50*, 17953–17979. [CrossRef] [PubMed]
62. Bučko, T.; Hafner, J.; Lebègue, S.; Ángyán, J.G. Improved description of the structure of molecular and layered crystals: Ab initio DFT calculations with van der Waals corrections. *J. Phys. Chem. A* **2010**, *114*, 11814–11824. [CrossRef] [PubMed]
63. Tersoff, J.; Hamann, D.R. Theory of the scanning tunneling microscope. *Phys. Rev. B* **1985**, *31*, 805. [CrossRef] [PubMed]
64. Choudhary, K.; Garrity, K.F.; Camp, C.; Kalinin, S.V.; Vasudevan, R.; Ziatdinov, M.; Tavazza, F. Computational scanning tunneling microscope image database. *Sci. Data* **2021**, *8*, 57. [CrossRef]
65. Tao, K.; Stepanyuk, V.S.; Hergert, W.; Rungger, I.; Sanvito, S.; Bruno, P. Switching a single spin on metal surfaces by a STM tip: Ab initio studies. *Phys. Rev. Lett.* **2009**, *103*, 057202. [CrossRef] [PubMed]
66. Tersoff, J. Method for the calculation of scanning tunneling microscope images and spectra. *Phys. Rev. B* **1989**, *40*, 11990. [CrossRef]

67. Szulbinski, W.S.; Kincaid, J.R. Synthesis and spectroscopic characterization of zinc tetra(3,4-pyridine) porphyrazine entrapped within the supercages of Y-Zeolite. *Inorg. Chem.* **1998**, *37*, 5014–5020. [CrossRef]
68. Wang, B.; Engelhardt, V.; Roth, A.; Faust, R.; Guldi, D.M. n-*versus* p-doping of graphite: What drives its wet-chemical exfoliation? *Nanoscale* **2017**, *9*, 11632–11639. [CrossRef]
69. Hou, J.; Wang, Y.; Eguchi, K.; Nanjo, C.; Takaoka, T.; Sainoo, Y.; Arafune, R.; Awaga, K.; Komeda, T. Enhanced magnetic spin–spin interactions observed between porphyrazine derivatives on Au(111). *Commun. Chem.* **2020**, *3*, 36. [CrossRef]
70. Wang, Y.; Hou, J.; Eguchi, K.; Nanjo, C.; Takaoka, T.; Sainoo, Y.; Awaga, K.; Komeda, T. Structural, electronic, and magnetic properties of cobalt tetrakis (thiadiazole) porphyrazine molecule films on Au(111). *ACS Omega* **2020**, *5*, 6676–6683. [CrossRef]
71. Hou, J.; Wang, Y.; Eguchi, K.; Nanjo, C.; Takaoka, T.; Sainoo, Y.; Awaga, K.; Komeda, T. Inter-molecule interaction for magnetic property of vanadyl tetrakis(thiadiazole) porphyrazine film on Au(111). *Appl. Surf. Sci.* **2018**, *440*, 16–19. [CrossRef]
72. Cheng, M.; Zhang, Q.; Yang, C.; Zhang, B.; Deng, K. Photocatalytic oxidation of glucose in water to value-added chemicals by zinc oxide-supported cobalt thioporphyrazine. *Catal. Sci. Technol.* **2019**, *9*, 6909–6919. [CrossRef]